JOURNAL OF MATERIALS SCIENCE 18 (1983) 1389–1404

High temperature internal oxidation behaviour of dilute Ni–Al alloys*

H. HINDAM‡
Molecular and Materials Research Division, Lawrence Berkeley Laboratory, University of California, Berkeley, CA 94720, USA

D. P. WHITTLE†
Department of Materials Science and Mineral Engineering, University of California, Berkeley, CA 94720, USA

The internal oxidation of dilute Ni–Al alloys, either pure or containing small additions of tantalum or hafnium, was investigated at 1200° C in air. The advance of the precipitation zone followed a parabolic relationship at a slightly decreasing rate with increasing aluminium content. The presence of active elements had no appreciable effect on the growth rate. The precipitate shape, size and spacing depended upon the aluminium concentration and more significantly on the active element additions. The morphology varied from polyhedral crystallites and epitaxial platelets in the Ni–0.5 wt% Al alloy, to well defined cylindrical rods extending across the precipitation zone approximately normal to the reaction interface, in the alloys of higher aluminium content. An also continuous and similarly oriented plate-like morphology was observed in the active element-containing alloys. X-ray microanalysis indicated that the continuous precipitates consisted of $NiAl_2O_4$ and Al_2O_3. The former phase comprised approximately 65 ± 5% of the outer region of the precipitation zone. Aluminium depletion in the alloy ahead of the precipitation front and a consequent enrichment in the form of oxide within the reaction zone inferred that growth was controlled by simultaneous outward aluminium and inward oxygen diffusion. No correlation was found between either the growth rate or oxygen permeability and the distribution of the precipitates. It was, therefore, concluded that the interfacial boundaries were ineffective in accelerating oxygen transport at this elevated temperature.

1. Introduction

The γ-NiAl solid solution phase has been the subject of several oxidation studies [1–7]. At least during an incipient stage dependent upon aluminium content, alloys within this phase field oxidized parabolically in air- or oxygen-rich atmospheres forming an external duplex scale consisting of outer and inner layers of aluminium-doped NiO and $NiO–NiAl_2O_4$ aggregates, respectively, and an aluminium-depleted alloy zone containing $NiAl_2O_4/Al_2O_3$ precipitates. A previous investigation [7] suggested that the growth of the subscale was controlled by inward oxygen diffusion at a rate which was enhanced by the incoherent boundaries between the precipitates and alloy matrix. The relative contribution of the boundary transport, however, diminished rapidly with temperature in the range of 800 to 1100° C. The

*Presented at the 34th Pacific Coast Regional Meeting of the American Ceramic Society, Newport Beach, California, October 1981.

‡Present address: National Research Council Canada, Industrial Materials Research Institute, 750 Bel-Air, Montreal, Quebec, Canada.

†Since the submission of this paper we have heard with regret of the death of Professor Whittle and would like to acknowledge his significant contributions to the subject of materials science.

0022–2461/83 $03.00 + .12

objective of the present study was to quantitatively assess the role of boundary transport, if any, at a higher temperature (1200° C), and its possible influence on the reaction mechanism by directly examining the relationship between the growth rate and morphology of the precipitate. The variation of the alloy aluminium content and the addition of active elements (tantalum and hafnium) were effective in modifying precipitate shape, size and distribution. The present detailed microstructural observations complement those documented in a previous paper [5].

2. Experimental procedures and results

Alloys of nominal compositions 0.5, 2 and 4 wt % aluminium were cast by electrical resistance melting of 99.99 wt % pure nickel and aluminium pellets in recrystallized Al_2O_3 crucibles under an ultrapure helium atmosphere. The cylindrical ingots were homogenized at 1300° C overnight in the same furnace. The Ni–2 wt % Al ingot also served as a master alloy for preparing the active-element containing compositions. 99.999 wt % pure hafnium powder and small strips sheared from a tantalum foil of similar purity were used to make 1% additions to the alloy. Rectangularly shaped specimens, approximately 15 mm × 12 mm × 3 mm, were cut, metallographically polished with SiC abrasive papers down to ~ 30 μm grit size and finally ultrasonically cleaned in distilled water. They were oxidized in static air at 1200° C. Layer thickness measurements were carried out on conventionally-prepared metallographic cross-sections using an optical microscope. A scanning electron microscope served for detailed microstructural observations on deeply etched specimens which were prepared by partial selective alloy dissolution in a 10 vol% Br_2–CH_3OH solution at ~ 30° C, a technique devised to examine the morphology of internal precipitates [5].

2.1. Microstructure

With the exception of the Ni–4 wt % Al alloy, as discussed later, all other compositions exhibited uniform internal oxide penetration even in the vicinity of alloy grain boundaries. However, an additional growth feature was the growth of a relatively denser population of precipitates at these alloy grain boundary locations, in the form of sheaths enveloping the alloy grains. This behaviour is documented in Figs. 1a to e. The close-up photographs, Figs. 1d and c, revealed the rather porous structure of these grain boundary precipitates. The latter observation in addition to uniform unaffected penetration at the vicinity of alloy grain boundaries are confirmatory evidence that the sheaths were ineffective in impeding inward oxygen diffusion and the advance of the internal precipitation front.

2.1.1. Pure alloys

Two distinct morphologies were discernible in the Ni–0.5 Al alloy (Figs. 2a to d): polyhedral crystallites in preponderance to rectangular platelets (see micrographs in Figs. 2c and d). The latter particles, which were confined to the inner region of the subscale (Fig. 2a), assumed defined orientations within each alloy grain (Figs. 2a, b and d). The relative enrichment of alloy grain boundaries with precipitates was accompanied by denudation of contiguous regions within the grains (Fig. 2a). This morphological feature is better illustrated in a transverse section normal to the growth direction at a triple alloy grain boundary intersection (Fig. 2b).

Only cylindrical, rod-like precipitates were observed in the Ni–2 wt % Al [5] and Ni–4 wt % Al alloys. This unique morphology is documented for the latter composition in Figs. 3a to d by sections along and across the precipitates. The rods extended along the precipitation zone generally normal to the reaction interfaces inferring epitaxial-free growth unlike the platelets formed in the Ni–0.5 wt % Al alloy. The occasional coalescence of two or more rods is evident in Fig. 3b.

Subsequent to a relatively short initial stage of uniform penetration, discontinuous Al_2O_3 films developed randomly at the precipitation front in the Ni–4 wt % Al alloy and spread laterally to encompass the internal oxidation zone inhibiting further rod growth. The structure of this barrier film (Figs. 3c and d) should be compared with the ineffective grain boundary oxide sheath, shown in Figs. 1d and e. It is evident that the former, which was not associated with alloy grain boundaries, grew laterally by precipitation of oxide in the alloy region adjoining the rods.

2.1.2. Active element containing alloys

In contrast to the rod-like precipitates formed in the pure Ni–2 wt % Al alloy, the addition of tantalum or hafnium led to a marked morphological change. The oxide particles in both the active elements containing alloys exhibited a

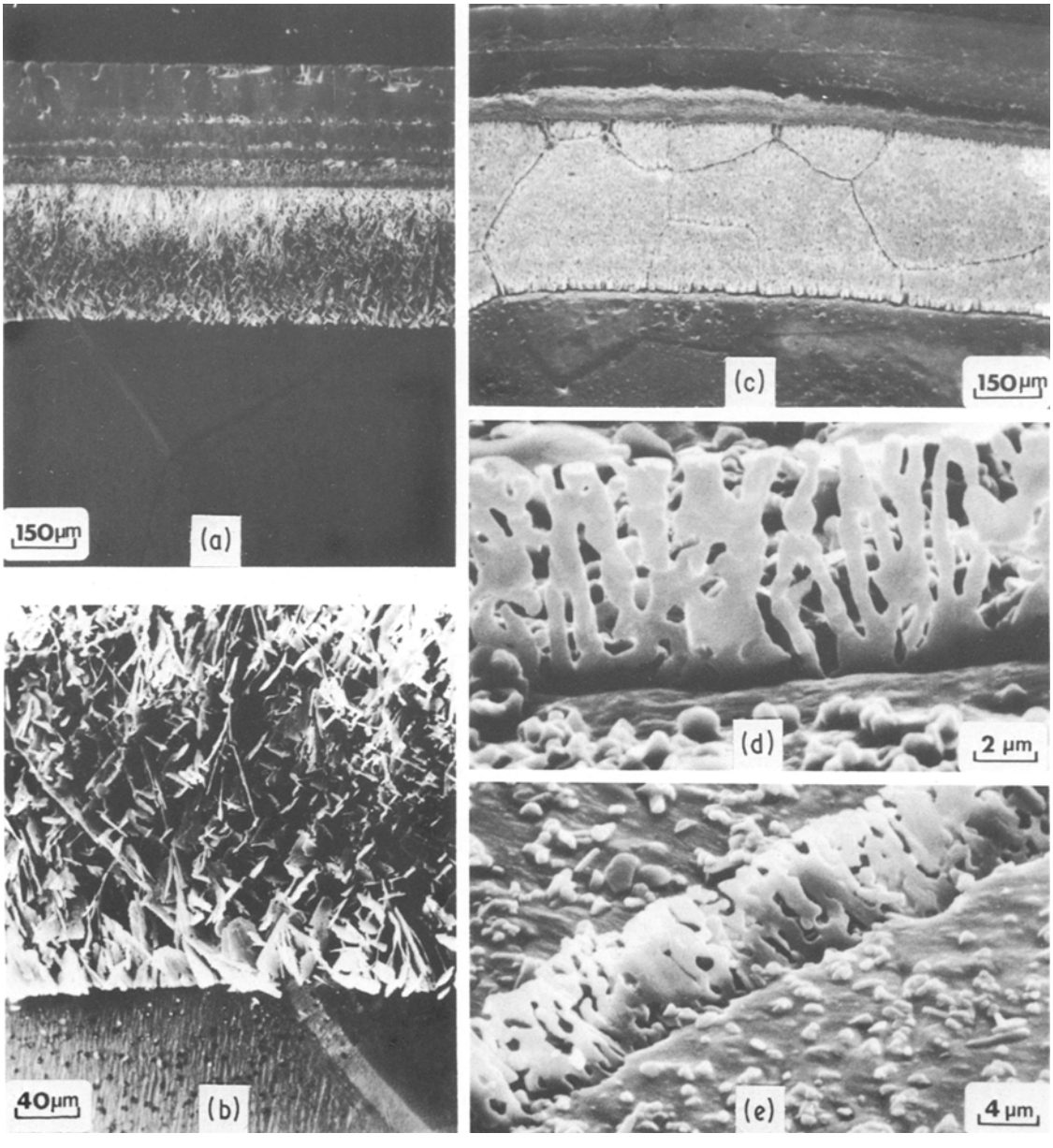

Figure 1 Internal oxide morphology at the vicinity of alloy grain boundaries illustrating uniform penetration and denser oxide population: (a) and (b) Ni–2 wt % Al–1 wt % Ta, (c) Ni–2 wt % Al–1 wt % Hf, (d) and (e) microstructure of grain boundary precipitates in the Ni–0.5 wt % Al alloy.

distinct rectangular plate-like structure as shown in Figs. 4 and 5, although this was less defined in the hafnium containing alloy. Similarly to the other compositions, alloy grain boundary decoration by formation of denser precipitates could be discerned (Figs. 4a and 5a); nevertheless, as pointed out earlier, no evidence was found to indicate that the advance of the precipitation front was affected by the development of these localized oxide-rich regions. In fact, the precipitates can be seen to extend without any interference across the boundary sheaths (Fig. 4b). As with the pure alloy, the plate-like particles grew as a continuous phase throughout the precipitation zone, perpendicular to the reaction interface. The platelets were randomly oriented throughout the alloy matrix and apparently intersected at various inclinations, including merging to form large slabs (Figs. 4c and d).

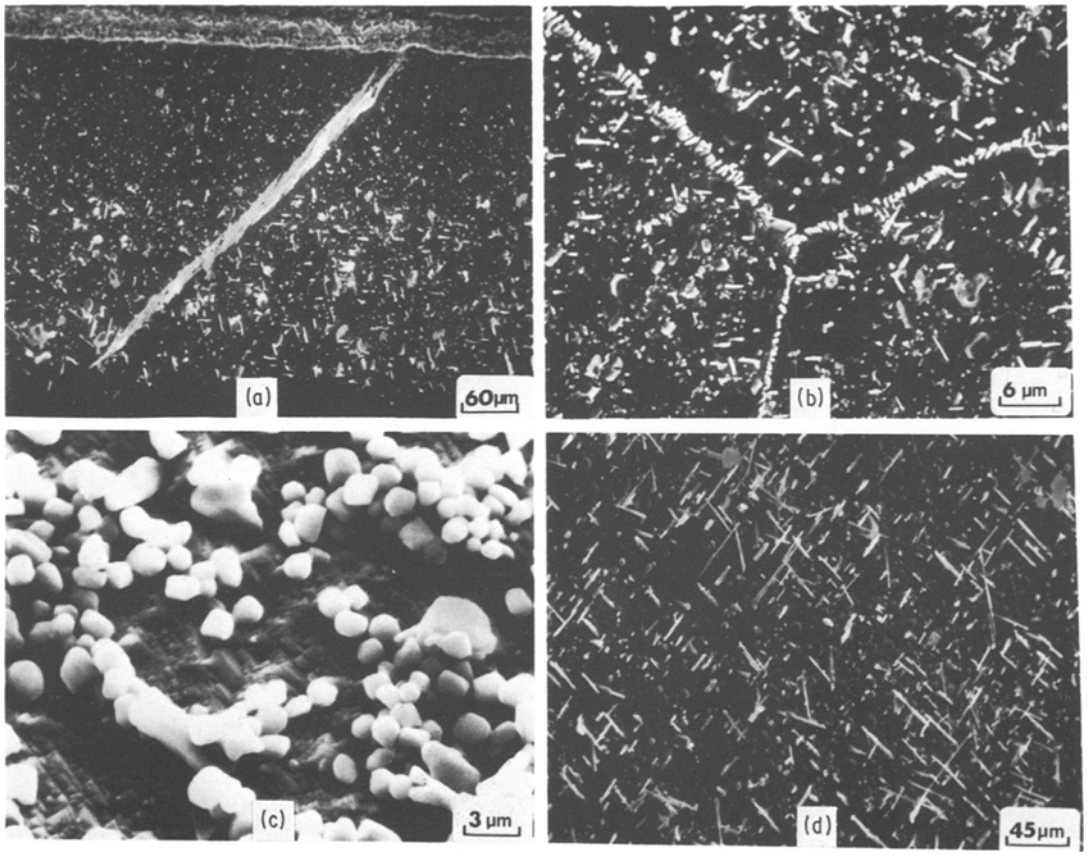

Figure 2 Internal oxide morphology in the Ni–0.5 wt % Al alloy: (a) cross-section, (b) transverse section at a triple grain boundary intersection, (c) polyhedral crystallites at the outer internal oxidation zone, (d) sporadically distributed spherical and oriented platelets in the inner region.

2.2. Composition and phase distribution

The determination of the composition of the particles within the alloy internal oxidation zone was based on energy dispersive X-ray microanalysis. The objective was to estimate the relative amount of the $NiAl_2O_4$ and Al_2O_3 phases. To minimize interference from the substrate, the measurements were performed on deeply etched specimens. Nickel and aluminium Kα X-ray maps for the rod-like precipitates in the Ni–4 wt % Al alloy are included in Fig. 6. The denudation of nickel and consequent enrichment of aluminium in the inner part of the particles adjacent to the precipitation front inferred that Al_2O_3 comprised approximately 35 ± 5% of the inner part of the subscale, whereas the rest was occupied by the spinel phase. No demarcation in the precipitate morphology was apparent at the transition "boundary" between the two phases.

Conclusions based on these measurements were considered tentative since it was realized that the X-ray yield can be significantly influenced by structural irregularities, absorption and excitation of the underlying, essentially pure nickel substrate. Nonetheless, deeply etched tapered sections at a small inclination with the sample surface showed a distinctive colour contrast which supported the above conclusion. The spinel phase appeared as light blue whereas Al_2O_3 was light grey. The present results agreed in principle with the recent measurements of several investigators [7, 8].

As evidenced by the X-ray maps shown in Fig. 7, the relative $NiAl_2O_4/Al_2O_3$ thickness was preserved in the hafnium- as well as tantalum-containing alloys. The active elements were uniformly distributed in the subscale zone; however, no definite conclusion could be reached with respect to whether they were dissolved in the oxide or alloy matrix or existed as discrete small oxide particles.

2.3. Growth kinetics

The typical overall scale morphology on the γ-NiAl solid solution alloys is illustrated in Fig. 8. Since

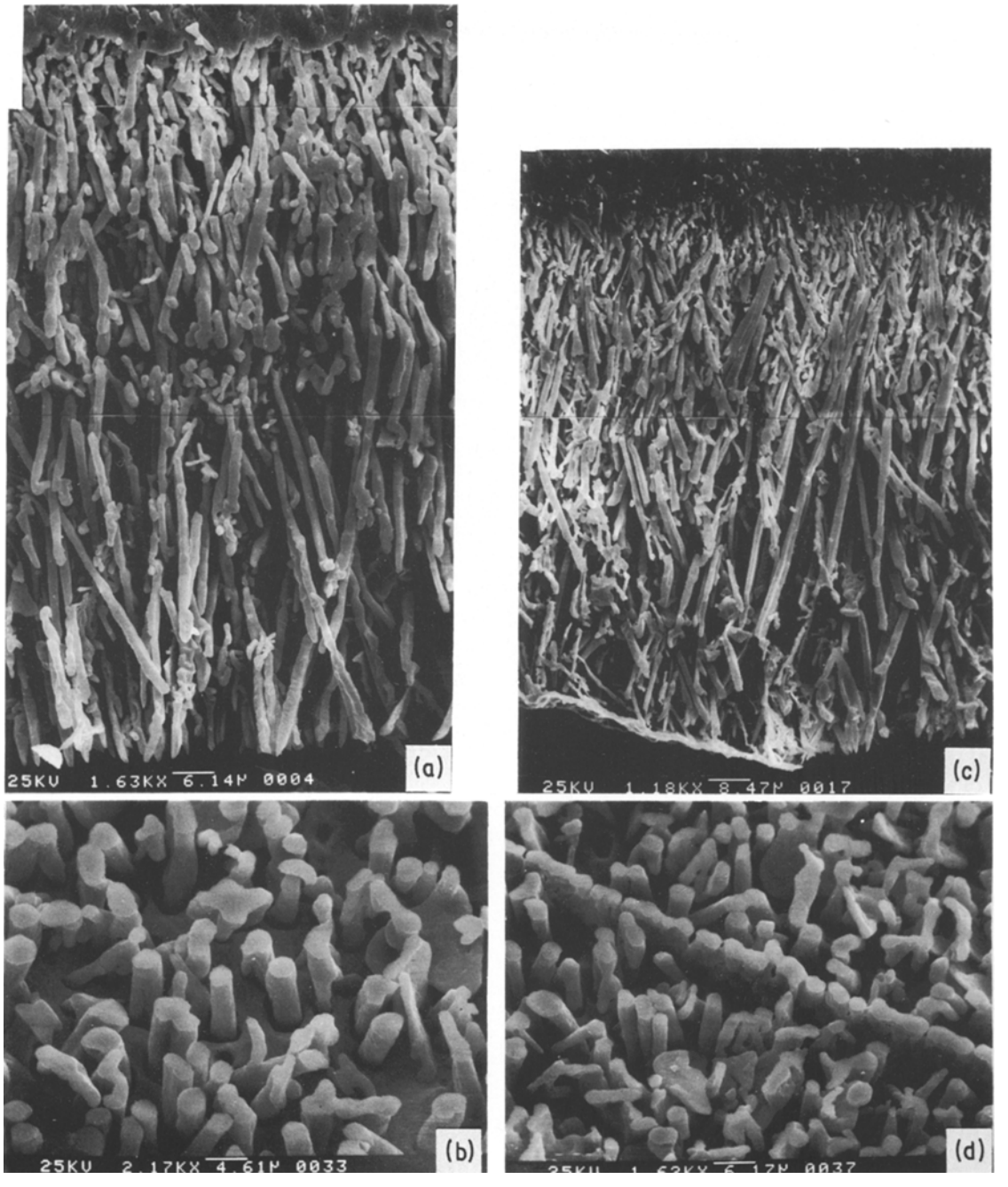

Figure 3 Internal oxide morphology in the Ni–4 wt % Al alloy: (a) and (b) longitudinal and transverse sections across the cylindrical rod-like precipitates, respectively, (c) and (d) similar sections illustrating the development of a continuous Al_2O_3 film at the precipitation front.

the $NiAl_2O_4$ precipitates extended in the external NiO scale forming a two-phase layer [5], the inner/outer layer interface was considered as a marker for the original alloy surface and all thickness measurements were made relative to that datum. As reported earlier, uniform internal oxide penetration was always observed, except in the Ni–4 wt % Al alloy during the later stages when lateral, discontinuous Al_2O_3 films developed at the precipitation front. In this case, only locations where uniform penetration was still observable, were considered for evaluation of the growth

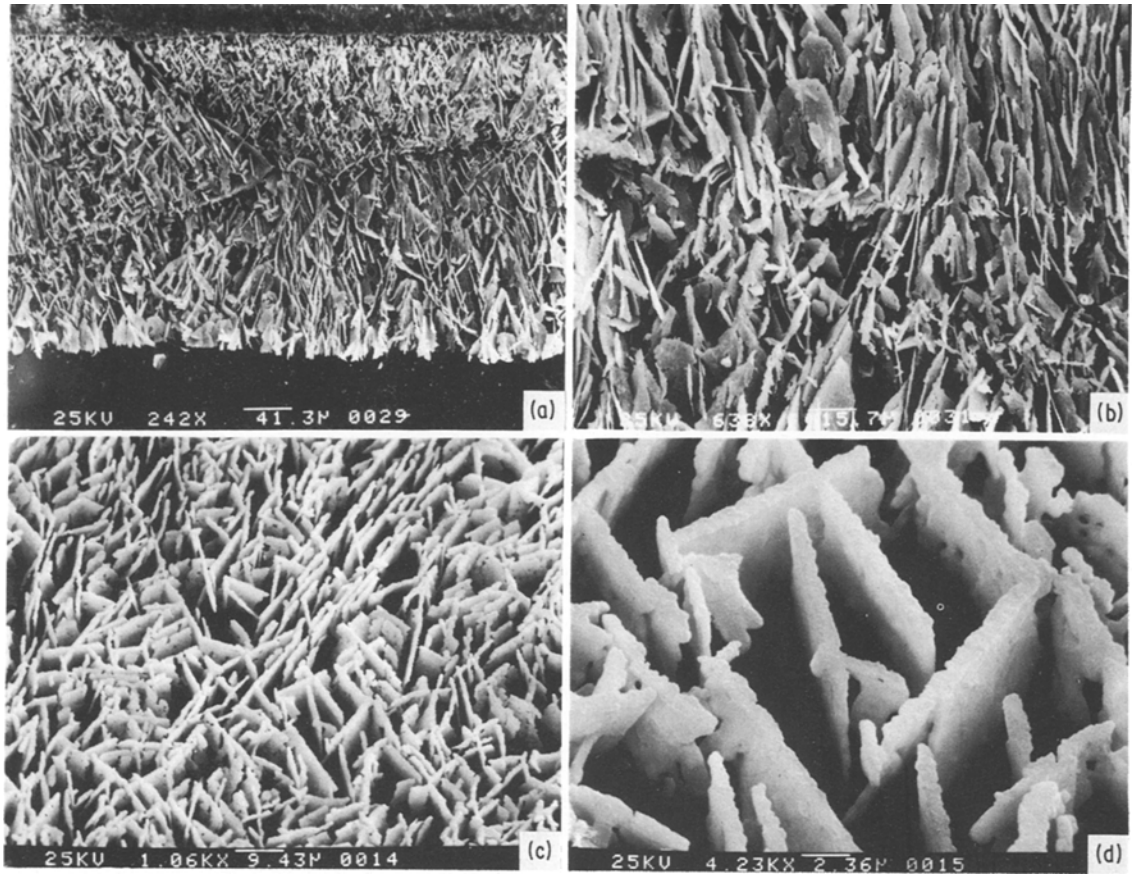

Figure 4 Internal oxide morphology in the Ni–2 wt % Al–1 wt % Ta alloy: (a) cross-section, (b) structural details in the vicinity of alloy grain boundary precipitates, (c) and (d) transverse sections across depicting a plate-like morphology.

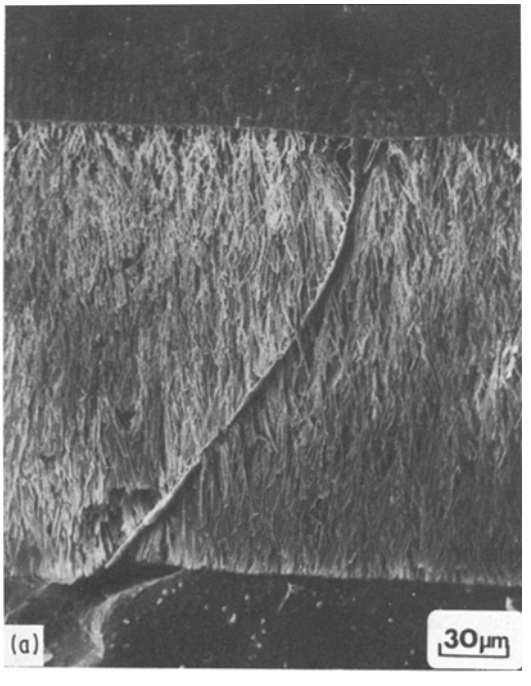

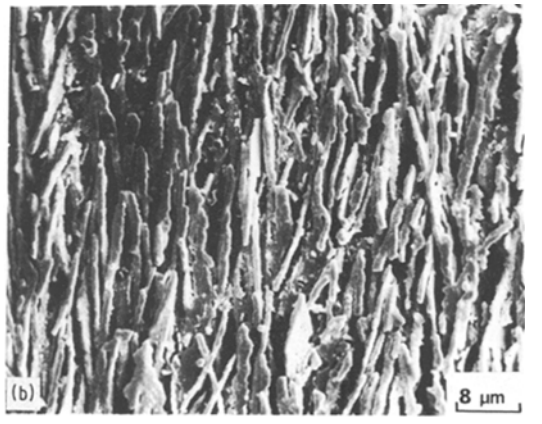

Figure 5 Internal oxide morphology in the Ni–2 wt % Al–1 wt % Hf alloy: (a) cross-section, (b) close-up view of the precipitates.

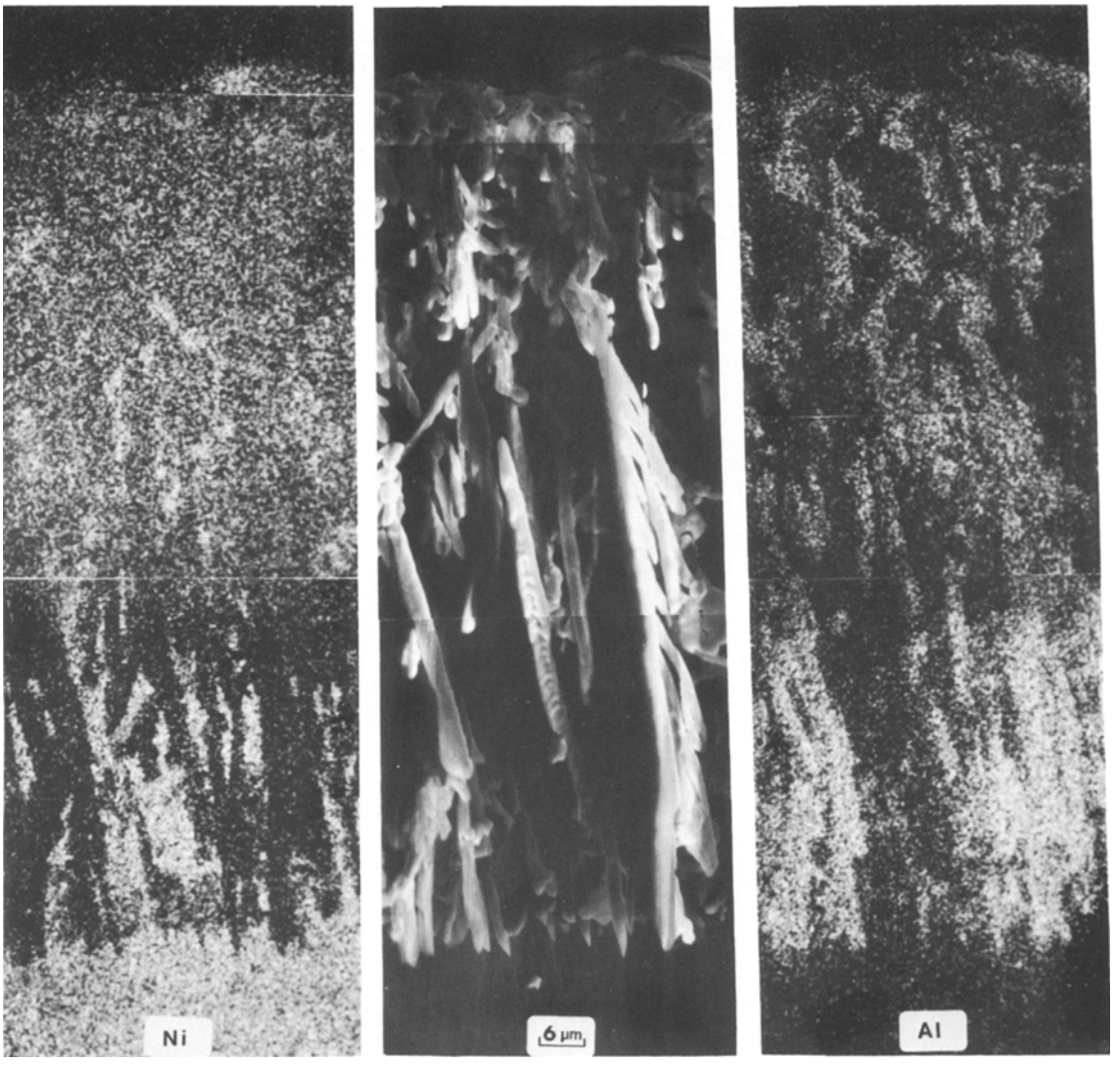

Figure 6 Nickel and aluminium X-rays maps of the rod-like precipitates in the Ni–4 wt % Al alloy.

kinetics. The results of these measurements are shown in Fig. 9 as a plot of precipitation zone thickness, ξ, against the square root of time, $t^{1/2}$. The advance of the precipitation zone is thus, approximately, described by a parabolic relationship in all cases. In the pure alloys, the rate constants decreased slightly with increasing aluminium content. It is evident that the addition of tantalum or hafnium to the Ni–2 wt % Al alloy did not affect the growth rate significantly. The measured rate constants are included in Table I.

2.4. Size and spacing distributions

For selected alloy compositions, the particle size and spacing were evaluated from sections parallel to the original alloy surface where the precipitates existed as $NiAl_2O_4$. This was confirmed by the characteristic light blue colour of this phase which became observable after extended deep etching. The spacing was defined as the centre to centre distance between nearest neighbours. The measurements, which were made at random locations, included at least 100 particles. The results are shown in Fig. 10. Typical transverse sections taken at the same magnification for all alloy compositions are included in Fig. 11 for a better visualization. A remarkable conspicuous difference in the distribution of the precipitates is evident. The data, included in Fig. 10, were based on micrographs similar to Fig. 11 but at magnifications ranging from 4K (particle spacing) to 10K (particle size).

TABLE I Experimental and calculated data for the internal oxidation of Ni–Al alloys

Alloy composition	Al atom fraction, N_{Al}	Precipitate growth rate constant, k ($\times 10^4$ cm sec$^{-1/2}$)	Average particle size, $\bar{d}$ (μm)	Average particle spacing, $\bar{S}$ (μm)	Volume fraction, V_f calculated		Fractional surface coverage, A_f or V_f measured	Oxygen permeability, $N_O^S D_O$ ($\times 10^{10}$ cm^2 sec^{-1})
					Al_2O_3	$Ni_2Al_2O_4$		
Ni–0.5 wt % Al	0.011	1.94	–	–	0.02	0.032	0.14	0.9
Ni–2 wt % Al	0.043	0.83	1.26 ± 0.04	3.3 ± 0.12	0.08	0.12	0.27	1.3
Ni–4 wt % Al	0.083	0.61	4.15 ± 0.1	6.6 ± 0.25	0.155	0.24	0.35	1.8
Ni–2 wt % Al–1 wt % Ta	0.043	1.04	$L = 5.5 \pm 0.3$ $W = 0.5 \pm 0.01$	–	–	–	0.36	1.8
Ni–2 wt % Al–1 wt % Hf	0.043	1.04	–	–	–	–	0.40	1.8

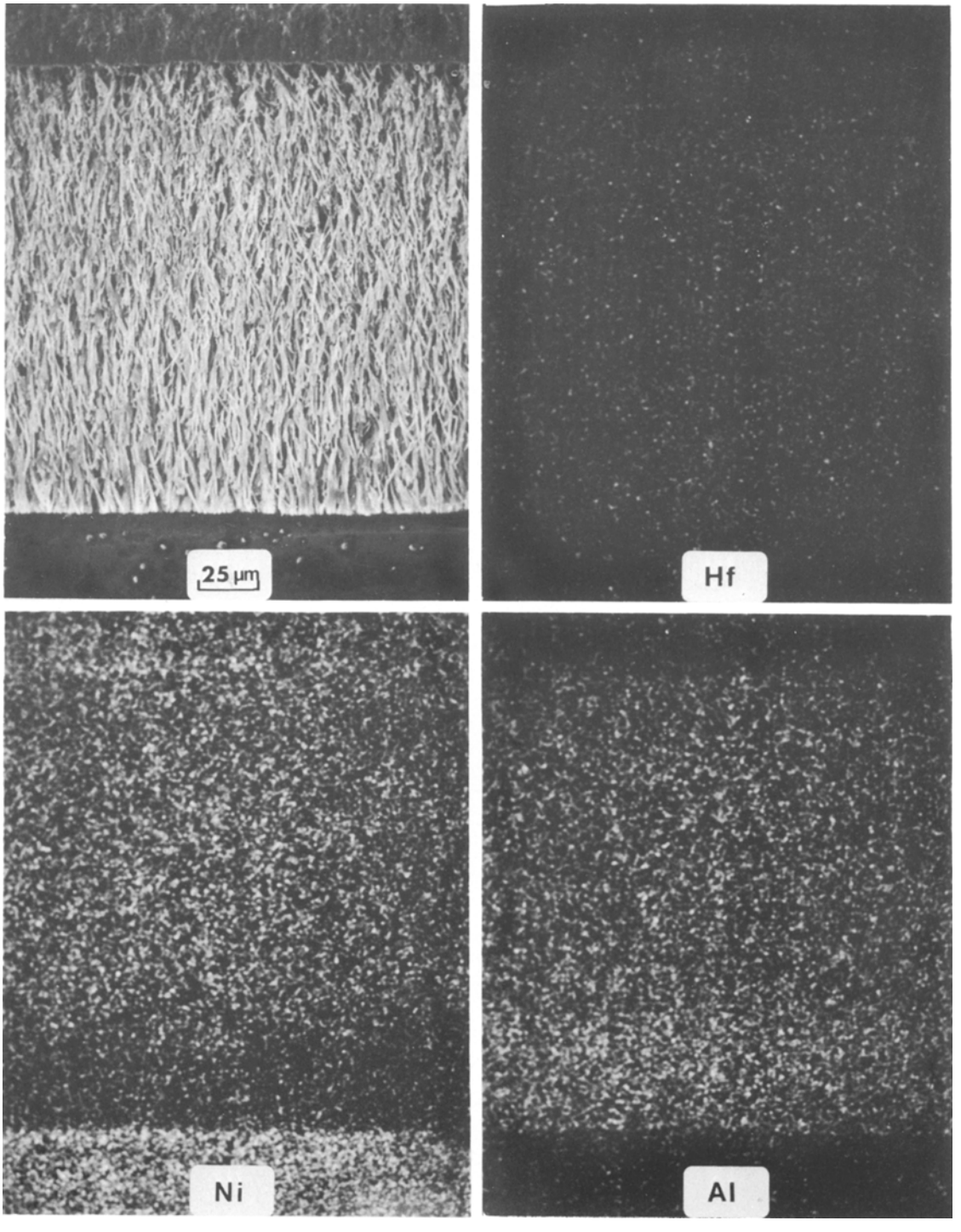

Figure 7 Hafnium, nickel and aluminium X-ray maps of the precipitation zone in the Ni–2 wt % Al–1 wt % Hf alloy.

The diameters of the rod-like precipitates in the Ni–2 wt % Al alloy showed very little variation as evidenced by the very sharp population density/size curve in Fig. 10. Furthermore, the rods were well spaced apart and there was virtually no overlap between their size and spacing distributions. In contrast, the precipitate rod diameters in the Ni–4 wt % Al alloy showed considerable spread, and this overlapped considerably with the very variable inter-rod separation. This finding, coupled

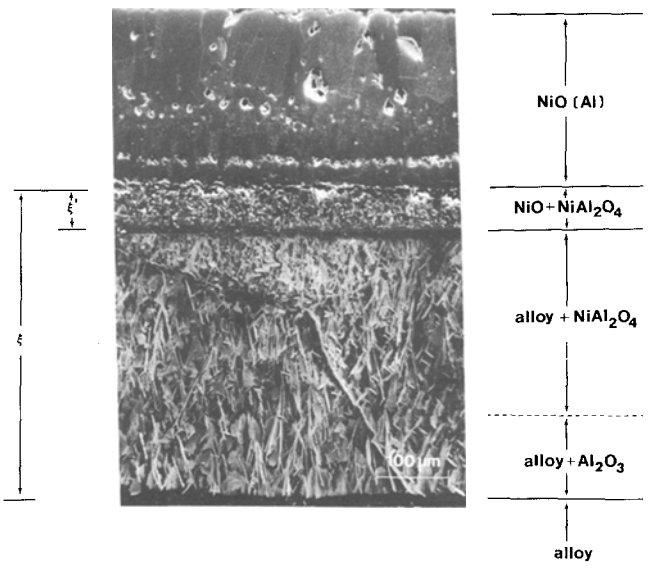

Figure 8 Overall scale morphology on the Ni–2 wt % Al–1 wt % Ta alloy.

with the metallographic observations discussed earlier, substantiate the impingement model which was proposed [5] to account for the transition from internal precipitation to continuous film formation in the aluminium-rich (Al $\gtrsim$ 4 wt %) alloys.

In the case of the tantalum-containing alloy, the platelet-like precipitates were uniform in width (0.5 μm), but there was considerable variation in their length. The latter dimension is included in Fig. 10. The average particle size and spacing are given in Table I.

2.5. Discussion and conclusions

The observed scale morphology is consistent with the thermodynamic constraints imposed by phase equilibria in the Ni–Al–O system. Indeed, a "virtual" diffusion path can be traced on the pertinent phase diagram [9] to represent this scaling behaviour [10]. The nickel-rich region of an isothermal section (1000° C) is reproduced in Fig. 12 on a logarithmic scale to include equilibria involving alloys with extremely small aluminium content which would correspond to the com-

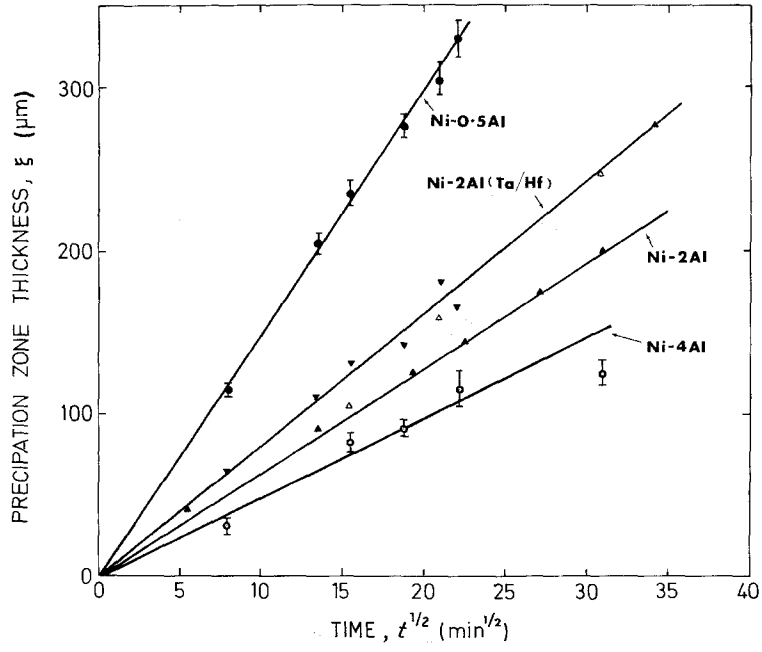

Figure 9 Parabolic plot of internal oxide growth.

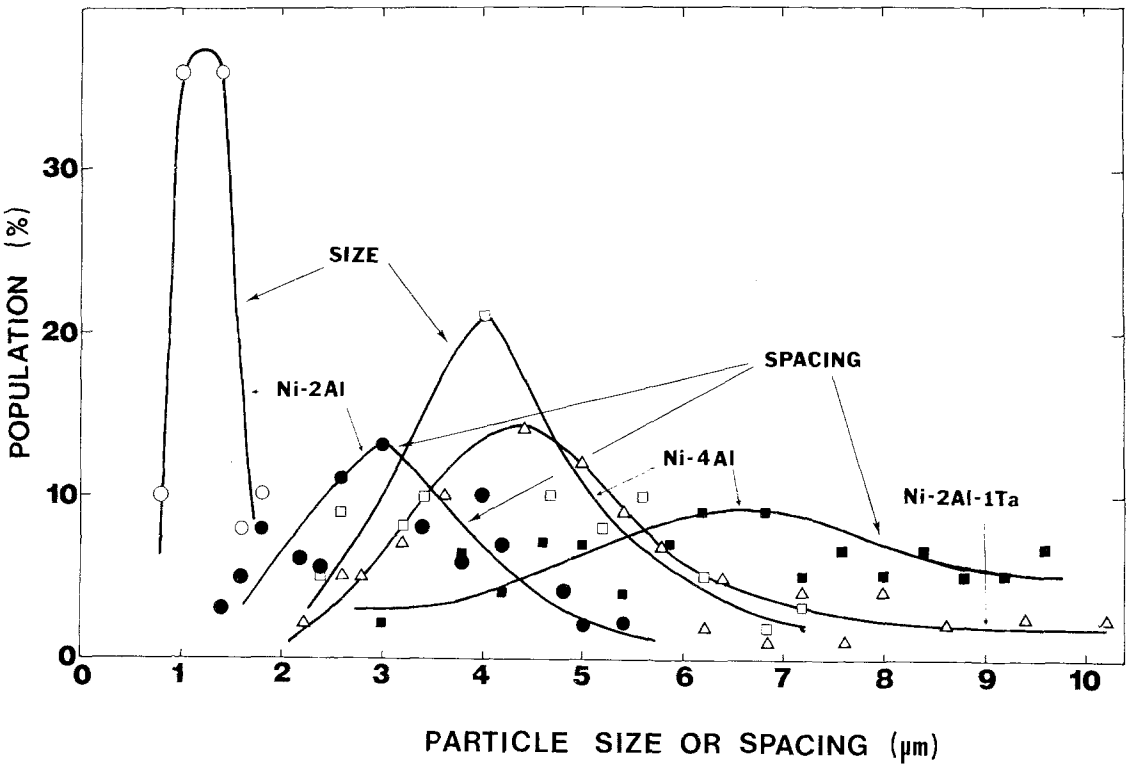

Figure 10 Precipitate size and spacing distributions.

position at the reaction front upon the precipitation of Al_2O_3. The sloping lines represent the following equilibria:

$$2\,Al\,(alloy) + 3/2\,O_2 = Al_2O_3(s) \quad (1)$$

$$Ni\,(alloy) + 2.54\,Al\,(alloy) + 2.405\,O_2 = NiAl_{2.54}O_{4.81}(s) \quad (2)$$

with

$$x_{Al}P_{O_2}^{3/4} = \gamma_{Al}^{-1} \exp\left[\frac{\Delta G^\circ_{Al_2O_3}}{2RT}\right] \quad (3)$$

and

$$x_{Al}(1-x_{Al})^{1/2.54}P_{O_2}^{2.405/2.54} = \gamma_{Al}^{-1} \exp\left[\Delta G^\circ_{NiAl_{2.54}O_{4.81}}/2.54RT\right] \quad (4)$$

respectively, where T is the temperature, P_{O_2} is the oxygen potential and R is the gas constant. The standard Gibbs energy of the formation, G, of the spinel phase ($NiAl_{2.54}O_{4.81}$) co-existing with NiO, was measured with respect to NiO and Al_2O_3 [9]. This was converted to a value corresponding to the above equation using $\Delta G^\circ_{Al_2O_3}$ and ΔG°_{NiO} from "JANAF Thermochemical Tables" [11]. Assuming Henrian behaviour, the activity coefficient of aluminium in the γ-NiAl solid solution was taken as 8×10^{-7} [12]. The oxygen potentials corresponding to the invariant three phase equilibria $\gamma NiAl$–$NiAl_{2.54}O_{4.81}$–Al_2O_3 and NiO–$NiAl_{2.54}O_{4.81}$–Al_2O_3 were 4.9×10^{-13} and 3.8×10^{-11} atm, respectively. The dissociation pressure of NiO in contact with pure nickel at this temperature was 5.4×10^{-11} atm. A schematic diffusion path is traced on Fig. 12. It was constructed assuming that the ratio of Al:Ni in the internal oxidation zone, and the inner layer of the scale, was identical with the bulk alloy. In fact, as discussed below, enrichment of aluminium in the internal oxidation zone (and presumably the inner scale layer) was evident, together with a corresponding depletion in the alloy immediately ahead of the precipitation front. However, this would not qualitatively affect the present argument, which is that in order to satisfy thermodynamic criteria, the composition of the precipitates must abruptly shift from Al_2O_3 in the region of the precipitation front to $NiAl_2O_4$ towards the subscale/scale interface. Furthermore, it is anticipated that the relative $Al_2O_3/NiAl_2O_4$ thickness would increase with aluminium content, although it must be emphasized that the length of the diffusion path within a particular phase region does not necessarily have any direct relationship

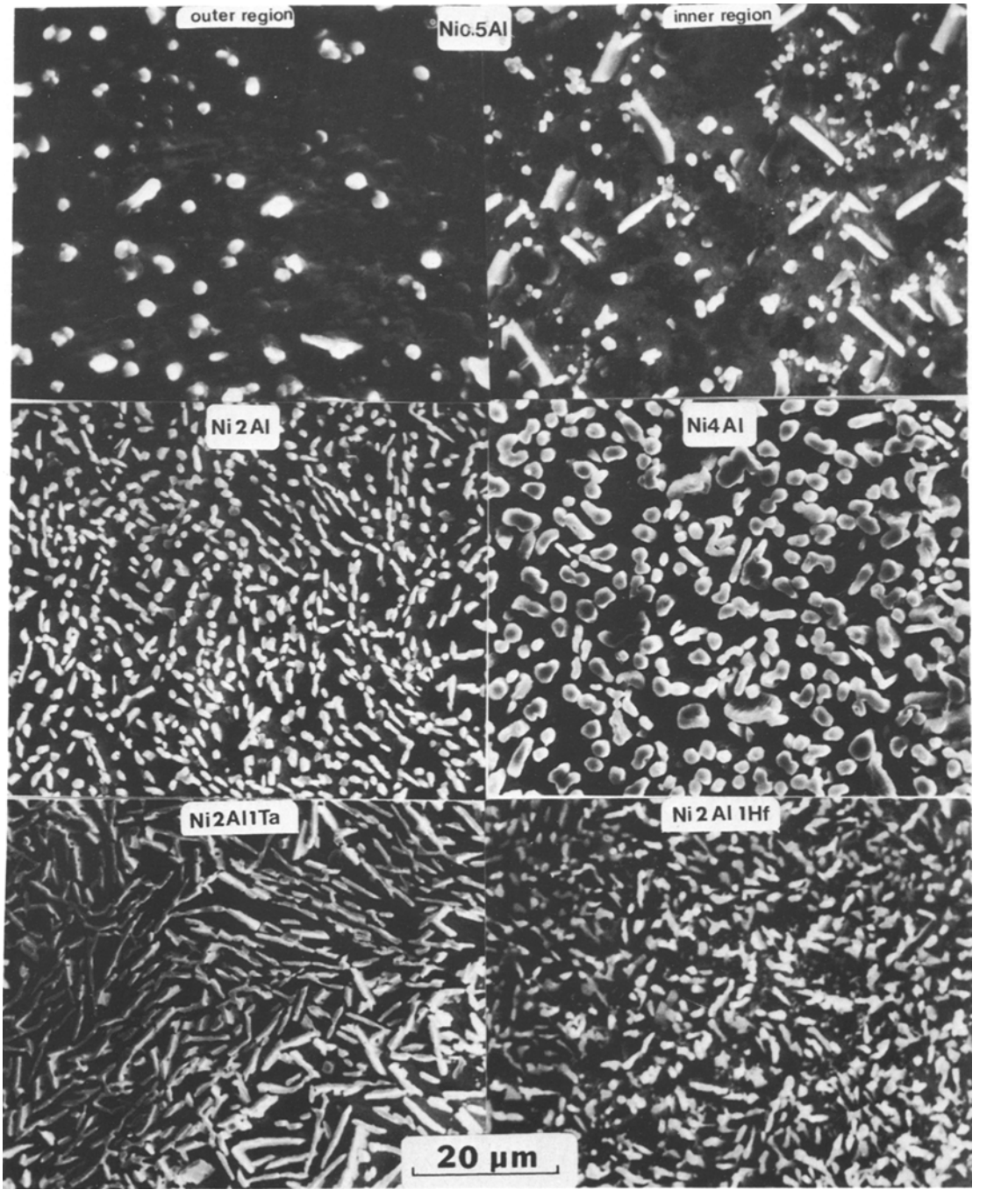

Figure 11 Transverse sections through the internal oxidation zone.

with the thickness of the region of that phase or phases in real space.

Before attempting a quantitative analysis, it is essential to first establish the growth mechanism. Depending on the relative diffusivities and solubilities of oxygen and solute metal in the alloy, two limiting cases are possible [13–15]: (i) if the oxygen permeability $N_O^s D_O \gg N_B^o D_B$, growth is controlled by oxygen diffusion and (ii) if these quantities are of similar magnitude, both oxygen and solute metal diffusion are rate controlling. A clear distinction between the two mechanisms is the formation of a metal denuded zone ahead of the reaction front and an equivalent enrichment

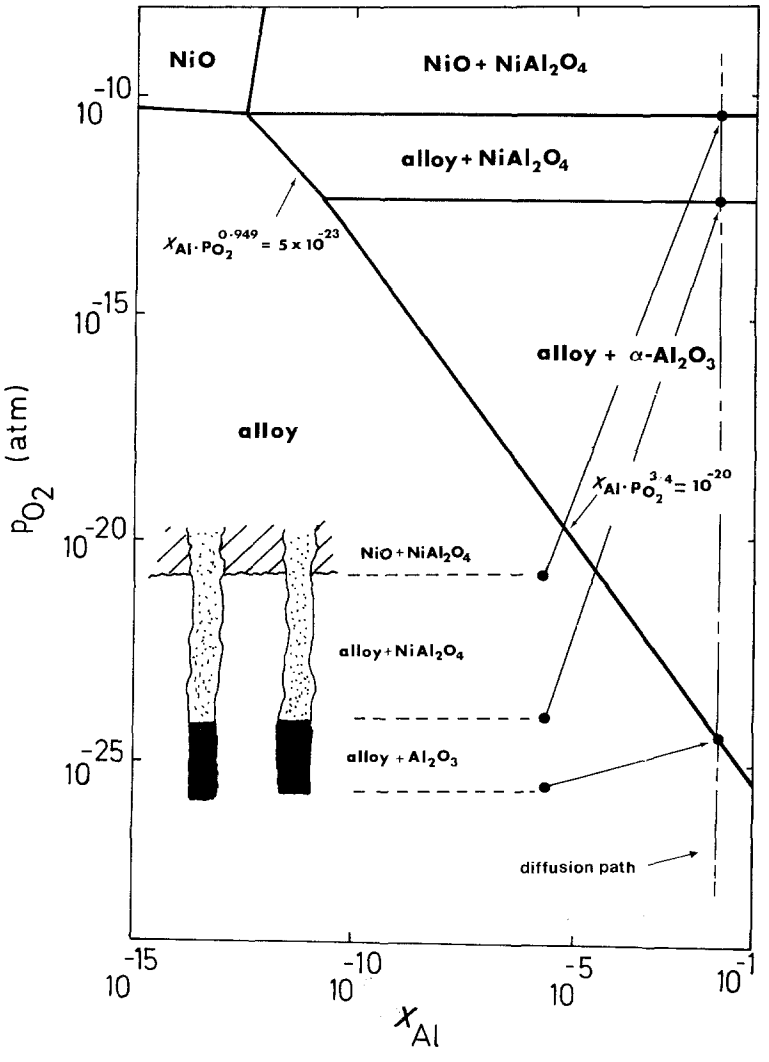

Figure 12 Nickel-rich region of the Ni–Al–O phase diagram at 1000° C, including a schematic diffusion path.

in the form of oxide within the precipitation zone in the latter case. Although aluminium depletion was detactable with electron probe microanalysis (EPMA), precise determination of the concentration profile was rather difficult because it occurred over a narrow distance. Therefore, identification of the prevailing mechanism was based on a comparison of the observed volume fraction of the precipitates with that calculated from a mass balance using metal and oxide densities assuming no aluminium diffusion in the alloy and no volume change accompanying internal oxidation. The results of these measurements, which were based on the linear intercept method [16], are shown in Fig. 13 along with the calculated values corresponding to $NiAl_2O_4$ or Al_2O_3. These data are also included in Table I. The calculated volume fraction does not depend significantly on the composition of the precipitates. The absence of structural discontinuities at the transition "boundary" between the two phases (Figs. 6 and 7) is consistent with this finding. Comparing the experimental and calculated values for the spinel phase (Fig. 13), it is evident that aluminium enrichment in all alloy compositions had occurred and that the presence of active elements (tantalum and hafnium) enhanced this process. The latter observation, in addition to the presence of an aluminium denuded zone in the alloy ahead of the precipitation front, inferred that at this elevated temperature the growth of the precipitates was controlled by oxygen as well as aluminium diffusion.

According to the classical internal oxidation model, the growth of the precipitates under the limiting case (ii), in the presence of an external scale as a source of oxygen, is described by [17]

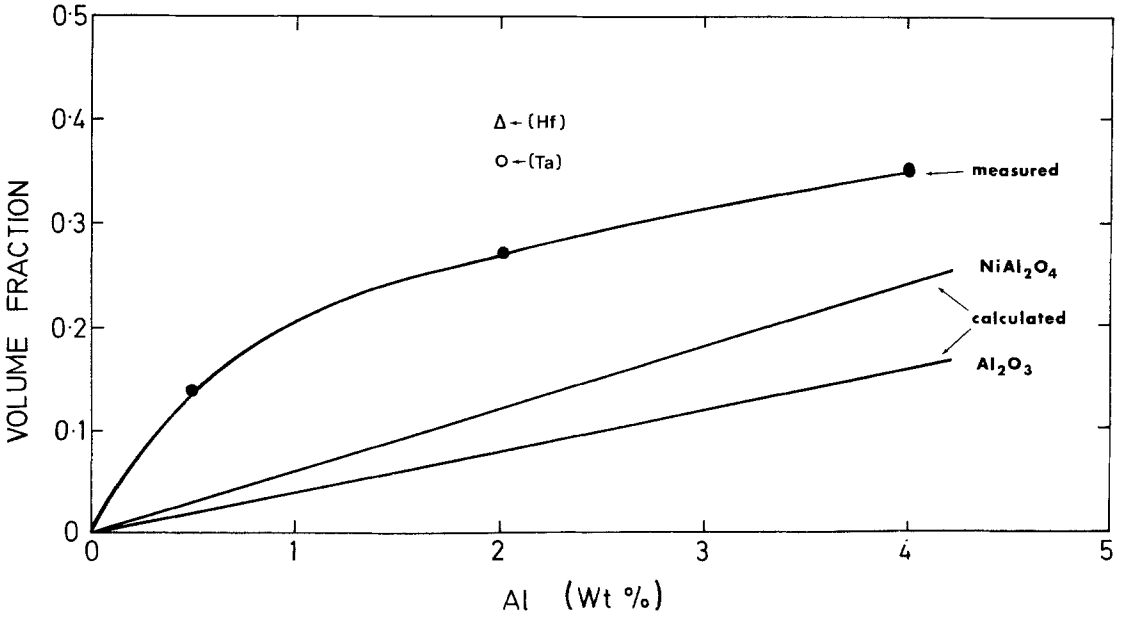

Figure 13 Volume fraction of oxide precipitates as a function of aluminium content.

$$\left[\xi\frac{(\xi-\xi')}{t}\right]^{1/2} = [k(k-k')]^{1/2} = \frac{\pi^{1/2}N_O^s D_O}{\nu_{eff}N_{Al}^o D_{Al}^{1/2}} \quad (5)$$

where ξ, and ξ' are the instantaneous depth of the internal oxidation zone and the scale/subscale interface relative to the original alloy surface (i.e. the recession of external scale), respectively: k, k' are the parabolic rate constants for the advance of the two interfaces. Note that the atomic ratio of oxygen to aluminium in the precipitates of the original equation has been changed to ν_{eff} to account for both spinel and Al_2O_3 being formed within the precipitation zone. In essence, ν_{eff} can be regarded as an adjustable parameter with limiting values of 1.5 and 2.0 corresponding to Al_2O_3 and $NiAl_2O_4$, respectively. Its actual value will depend on the relative thickness of the spinel and Al_2O_3 regions in the internal oxidation zone. Indeed, for the similar, but not identical, case where two oxides, e.g. BO_{ν_1} and BO_{ν_2}, can form internally, this functional dependence has been derived [18].

Since no inner spinel containing layer could be identified in the external scale formed on Ni–0.5 wt % Al alloy, k' is assumed to be negligible in this case. For the other alloys, $k' = 0.19 \times 10^{-4}$ cm sec$^{-1/2}$, independent of aluminium content. Using a value for the concentration-independent interdiffusion coefficient in γ-NiAl [19, 20] at this temperature of 1.4×10^{-9} cm^2 sec^{-1} and $\nu_{eff} = 2.0$, the oxygen permeability product $N_O^s D_O$ was calculated from Equation 5. Values are given in Table I, where it is evident that the oxygen permeability is virtually independent of aluminium concentration, or the presence of the reactive elements. Values range from 0.9 to 1.8×10^{-10} cm^2 sec^{-1}. It should be emphasized that the relative amount of the $Al_2O_3/NiAl_2O_4$ phases has no significant bearing on the precipitate growth rate or the calculated oxygen permeability values. This finding is in contrast to the behaviour of alloys at lower temperatures, where a strong dependence of the "apparent" $N_O^s D_O$ product on alloy aluminium content was found [7]. Values for a range of alloy compositions oxidized in 1 atm oxygen are shown in Fig. 14, where it is clear that the difference between the various alloy contents diminished with increasing temperature. Included also in Fig. 10 are values of $N_O^s D_O$ in "pure" nickel obtained by extrapolation of plots of $N_O^s D_O$ against (wt %) Al to 0% Al at the various temperatures [7], and values from independently measured solubilities [21] and diffusivity [22], although this latter work is rather dated. The present datum point for 1200° C fits closely with the extrapolated line through the low temperature oxidation data.

The model advanced for the dependence of the

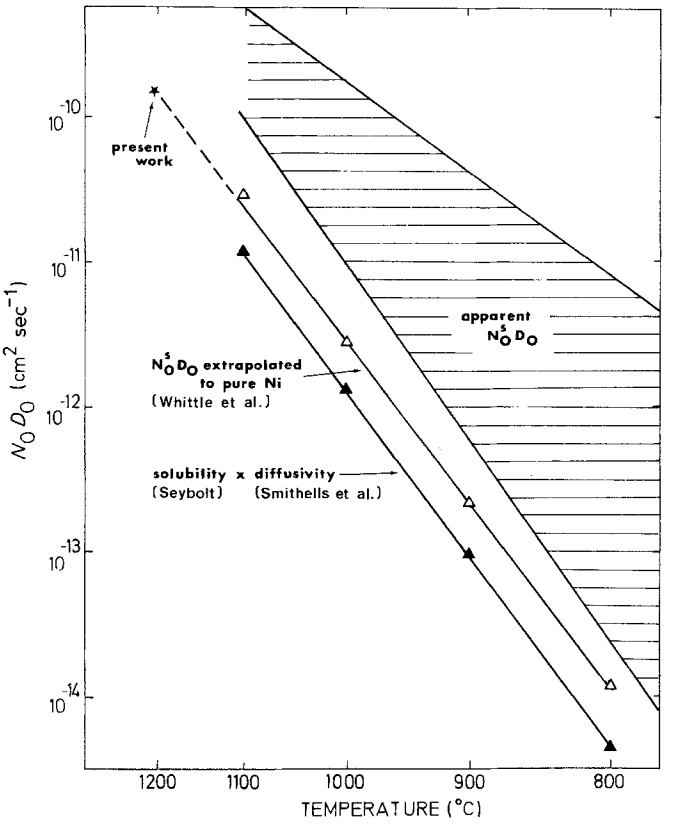

Figure 14 Arrhenius plot of the oxygen permeability product in γ-NiAl solid solution alloys.

permeability product on alloy aluminium content considered the contribution of the oxide precipitate/matrix interface in providing enhanced oxygen diffusivities, with the densities of these boundaries increasing with aluminium content, although this was not measured directly. In the present work, the apparent precipitate/alloy interfacial boundary density can be calculated using the measured distributions. For the three alloy compositions considered, the ratio of these quantities is given by

$$\left[\frac{4A_f}{\bar{d}}\right]_{\text{Ni—2 wt\% Al}} : \left[\frac{4A_f}{\bar{d}}\right]_{\text{Ni—4 wt\% Al}} : \left[\frac{2A_f(W+L)}{W \times L}\right]_{\text{Ni—2 wt\% Al—1 wt\% Ta}} \quad (6)$$

which upon substituting the appropriate values from Table I becomes

$$[2.5]_{\text{Ni—2 wt\% Al}} : [1]_{\text{Ni—4 wt\% Al}} : [5]_{\text{Ni—2 wt\% Al—1 wt\% Ta}} \quad (7)$$

where L is the side length and W is the width. This relatively small variation in boundary density in contrast to a remarkable difference in precipitate distribution, which arose from varying alloy composition and active element addition, stems from opposing factors, namely, alteration of particle shape, size and volume fraction. For instance, increasing the aluminium content or addition of active element led to an increase in precipitate volume fraction; however, the boundary density per particle was reduced due to increased particle size. Nevertheless, it is believed that the true boundary density would be significantly different since the boundary width depends on the degree of incoherency, and thence on particle size and shape.

In this latter context, it seems appropriate to consider briefly the factors involved. For other than the 0.5 wt % Al alloy, the internal precipitates always adopted the form of continuous rods or plates extending virtually completely right the way through the internal oxide zone. The reason for this is presumably related to the degree of supersaturation existing ahead of the precipitate zone. It was suggested [23] that oxygen diffuses ahead of the precipitate zone causing the concentration product $N_B N_O^v$ to exceed its equilibrium value at a finite distance ahead of the precipitation front.

Eventually, it becomes high enough to provide sufficient driving force to nucleate a new oxide particle. There were not sufficient data to carry out similar calculations in the present system, and it can only be assumed that because of the high stability of Al_2O_3 there is never sufficient oxygen diffusing ahead of the precipitation zone to produce significant supersaturation of the matrix with respect to oxide.

Thus, in conclusion, the virtual non-dependence of the oxygen permeability on alloy composition, albeit of a variation in interfacial boundary density, inferred that the latter did not enhance oxygen diffusion at high temperatures. The transition to an oxygen diffusion controlling mechanism at lower temperatures [7] was probably associated with a much finer and higher precipitate density.

Acknowledgements

This work was supported by the Director, Office of Energy Research, Office of Basic Energy Science, Materials Science Division of the US Department of Energy under Contract No. DE-AC03-76SF00098. Discussions with Professor W. W. Smeltzer, McMaster University were especially helpful.

References

1. J. S. WOLF and E. B. EVANS, *Corros.-NACE* 18 (1962) 129t.
2. W. C. HAGEL, *Corros.* 21 (1965) 316.
3. F. S. PETTIT, *Trans. Met. Soc. AIME* 239 (1967) 1296.
4. F. H. STOTT and G. C. WOOD, *Corros. Sci.* 17 (1977) 647.
5. H. HINDAM and W. W. SMELTZER, *J. Electrochem. Soc.* 127 (1980) 1622.
6. W. W. SMELTZER, H. HINDAM and F. A. ELREFAIE, Proceedings of the NACE Conference on High Temperature Corrosion, San Diego, California, March 1981 (National Association of Corrosion Engineers, Houston, Texas).
7. D. P. WHITTLE, Y. SHIDA, G. C. WOOD, F. H. STOTT and B. D. BASTOW, *Phil. Mag. A*, in press.
8. F. A. ELREFAIE and W. W. SMELTZER, *Oxid. Met.* 18 (1982) 407.
9. *Idem, J. Electrochem. Soc.* 128 (1981) 2237.
10. H. HINDAM, PhD thesis, "Microstructure and Growth of Al_2O_3 on Ni–Al Alloys", McMaster University (1979).
11. "JANAF Thermochemical Tables ", 2nd edn, edited by D. R. Stall and H. Prophet (National Bureau of Standards, Washington DC, 1971).
12. R. HULTGREN, P. D. DESAI, D. T. HAWKINS, M. GLEISER and K. K. KELLY, "Selected Values of the Thermodynamic Properties of Binary Alloys" (American Society for Metals, Metals Park, Ohio 1973) p. 191.
13. C. WAGNER, *Z. Elektrochem.* 63 (1959) 772.
14. R. A. RAPP, *Corrosion* 21 (1965) 382.
15. J. H. SWISHER, "Oxidation of Metals and Alloys", edited by D. L. Douglass (American Society for Metals, 1971) p. 235.
16. E. E. UNDERWOOD, "Metals Handbook" Vol. 8, edited by T. Lyman, 8th edn. (American Society for Metals, Metals Park, Ohio 1973).
17. F. MAAK, *Z. Metallkunde* 52 (1961) 545.
18. T. L. MEIJERING, *Adv. Mater. Res.* 5 (1971) 1.
19. J. D. WHITTENBERGER, *Met. Trans.* 3 (1972) 2010.
20. M. M. P. JANSSEN, *ibid.* 4 (1973) 1623.
21. A. V. SEYBOLT, quoted in "Metals Reference Handbook", edited by C. J. Smithells, 5th edn. (Butterworths, Borough Green, 1976).
22. C. J. SMITHELLS and C. E. RANSLEY, *Proc. Roy. Soc.* A155 (1936) 195.
23. G. BÖHM and M. KAHLWEIT, *Acta Met.* 12 (1964) 641.

Received 7 June
and accepted 16 July 1982